Title	Influence of trivalent doping on point and Frenkel defect formation in bulk chromium (III) oxide
Author(s)	Carey, John J.; Nolan, Michael
Publication date	2017-05-02
Original citation	Carey, J. J. and Nolan, M. (2017) 'Influence of trivalent doping on point and Frenkel defect formation in bulk chromium (III) oxide', Solid State Ionics, 307(Supplement C), pp. 51-64. doi: 10.1016/j.ssi.2017.04.016
Type of publication	Article (peer-reviewed)
Link to publisher's version	http://www.sciencedirect.com/science/article/pii/S0167273817302072 http://dx.doi.org/10.1016/j.ssi.2017.04.016 Access to the full text of the published version may require a subscription.
Rights	© 2017 Published by Elsevier B.V. This manuscript version is made available under the CC BY-NC-ND 4.0 license. http://creativecommons.org/licenses/by-nc-nd/4.0/
Embargo information	Access to this article is restricted for 24 months after publication by request of the publisher.
Embargo lift date	2019-05-02
Item downloaded from	http://hdl.handle.net/10468/4949

University College Cork, Ireland
Coláiste na hOllscoile Corcaigh

Influence of trivalent doping on point and Frenkel defect formation in bulk chromium (III) oxide

John J Carey, and Michael Nolan

Tyndall National Institute, University College Cork, Lee Maltings Complex, Dyke Parade, Cork, Ireland

John.carey@tyndall.ie , Michael.Nolan@tyndall.ie

Abstract:

Substitutional doping in metal oxides is a well-known approach to modifying properties such as ionic conductivity or activity in catalysis. Chromium (III) oxide is an attractive reducible material that has potential use as an oxygenation catalyst, and the fact that it maintains its integrity at high operating temperatures makes it useful for high temperature methanol synthesis and solid oxide fuel cells. Understanding the defect chemistry of Cr_2O_3 is important for rational catalyst design, in particular when the material is modified by isovalent doping. Density functional theory calculations with a Hubbard +U correction applied to the Cr 3d and O 2p states are used to investigate isovalent doping with Al^{3+}, Fe^{3+} and La^{3+} cations. Point defects including Cr and O vacancies, and Frenkel defects are investigated and the effect of cation doping on the defect formation energies in Cr_2O_3 is explored. Our calculations show that Cr Frenkel and peroxide point defects are the most favourable defects in undoped Cr_2O_3. Al^{3+} doping in Cr_2O_3 does not change the defect formation energies over undoped Cr_2O_3, and Fe^{3+} doping improves oxygen vacancy formation while greatly increasing the formation energies of other defects that are potential competing processes that may kill ionic conductivity. La^{3+} doping in Cr_2O_3 is found to also improve oxygen vacancy formation and induces a considerable decrease in the cost to form Cr vacancies and Frenkel defects. The modifications to the defect formation energies induced by these dopants in Cr_2O_3 can be used to impede formation of undesirable defects, thus enhancing ionic conductivity for oxygenation catalysis.

Keywords: Isovalent doping; density functional theory; catalysis; SOFC; metal oxide;

1.   Introduction:

The need for sustainable energy technologies becomes increasingly more prevalent with the decreasing supply of non-renewable fossil fuels, which will eventually become exhausted by the end of the century. To lessen our dependence on fossil fuels as an energy source, clean, efficient technologies based on renewable energy sources are required. Fuel cells are an alternative renewable energy technology as they can cleanly and efficiently produce electrical power from a variety of renewable fuel sources such as H_2, CH_4 and synthesis gas (mixture of CO and H_2). Solid oxide fuel cells (SOFCs) consist of a cathode, anode, electrolyte and interconnect materials operating at high temperatures (>1000K). Issues such as high overpotentials for the oxygen reduction reaction (ORR) in SOFCs require expensive ORR catalysts such as Pt metal, or high operating temperatures that can cause premature aging of the SOFC. Intermediate temperature SOFCs (IT-SOFC) that operate between 800K and 1000K are studied to lower the ORR by using mixed oxygen-ion-electron conducting (MIEC) cathode materials that increase the active region of the cathode. MIEC cathode materials allow bulk oxygen transport, as well as electronic conduction, and the oxygen mobility property determines the potential for using the material for IT-SOFCs. A material that has high oxygen mobility at elevated temperatures is crucial for redox processes in IT-SOFCS applications, and mobility that is governed by an oxygen vacancy hopping mechanism [1-3]. Oxygen vacancy formation is typically examined in metal oxide catalysis as a descriptor for candidate materials, and as an indicator for reducibility of the material. Improving the oxygen vacancy formation energy can enhance the ability of a material to transport oxygen for improved performance at lower temperatures.

Materials with the capacity to store and release oxygen are potential candidates for SOFCs since they have the ability to regulate the oxygen partial pressure which is crucial for the control of redox reactions, such as oxygen vacancy formation. In addition, oxygen storage and release

materials are used in three-way catalytic converters to remove gases such as CO or NO_x. Commercially, the most widely used oxygen storage material (OSM) is CeO_2-ZrO_2 as it is a highly reducible material that can easily form oxygen vacancies, and is therefore highly reactive for catalytic reactions on the surface and also displays good oxygen transport. The crucial step for this is the ability of Ce^{4+} cations to reduce to Ce^{3+} cations to facilitate oxygen vacancy formation which is also a key property for many reducible oxide catalysts such as TiO_2 (Ti^{4+} to Ti^{3+}) for photocatalysis or V_2O_5 (Vi^{5+} to V^{4+}) for a number of catalytic reactions. However the problem with CeO_2 based catalysts for SOFC applications is the inability to operate at moderate to high temperatures over extended periods.

A reducible oxide that can sustain high temperatures and pressures is chromium oxide (chromia), which has oxidation states that range from Cr^{2+} to Cr^{6+}, crystallising in different phases of CrO, Cr_2O_3, Cr_2O_5 and CrO_3.[4] The hexagonal corundum (α-Cr_2O_3) structure is the most thermodynamically stable phase and is a dielectric material with a wide band gap ($> 3eV$) that has both Mott-Insulator and charge transfer semi-conducting properties,[5, 6] which has been characterised by electron-energy-loss spectroscopy,[7] and X-ray photoemission spectroscopy.[8] Density functional theory calculations (DFT) with the generalised gradient approximation (GGA) have calculated the fundamental band gap in the range of 2.8eV – 3.1 eV,[9-15] and from a screened hybrid functional method the computed band gap is 3.31 eV.[16] Chromia is a magnetic material that displays anti-ferromagnetic ordering with alternating "-+-+" Cr cation layers.[12, 13] Defect formation in undoped Cr_2O_3 was explored using Mott-Littleton calculations which found that Cr and O vacancies are the dominant charge carriers.[17] DFT calculations have been presented using a Hubbard +U correction applied to the Cr 3d states to investigate intrinsic defects in Cr_2O_3, showing that charge neutral Cr Frenkel defects $[Cr_i^{\cdot\cdot} + V_{Cr}''']$ have the lowest formation energy while Cr vacancies are more stable than O vacancies.[9] The facile formation of vacancies in the undoped Cr_2O_3 material makes it a

promising candidate for a number of applications as cation and anion vacancies are useful for improved catalysis. Not only is chromia a potential candidate material for SOFCs,[18, 19] but it is an OSM material for a wide range of applications in oxygenation catalysis,[20-23] methanol synthesis,[24-26] an anode material for battery applications,[27, 28] as a gas sensor,[29] protective coatings,[30, 31] and adhesion promoters.[32] Since the reducibility of chromia is important for these applications, the formation of oxygen vacancies is a crucial step for ion conductivity and allowing the material to efficiently act as an active oxidising component.

Substitutional doping by replacing a Cr cation on its lattice site with a different metal dopant is an approach to alter the electronic properties of the host material, improving its reducibility, and has been extensively investigated for well-known oxides such as TiO_2[33-38] and CeO_2.[39-46] The changes in the local geometry as well as the change in electronic properties arising from the presence of the dopant can also facilitate oxygen vacancy formation in the host metal oxide. A metal dopant which has a valence state in its parent oxide that is lower than the host oxide is called a lower valence dopant (LVD), a dopant with a valence state in its parent oxide that is higher than the host material is a higher valence dopant (HVD) and a dopant with the same valence state as the host metal oxide is an isovalent dopant (IVD). In LVD doping of a +2 cation in Cr_2O_3, the spontaneous formation of a charge compensating oxygen vacancy releases two electrons into the host oxide which fill the holes present on the lattice oxygen anion.[15] This has been investigated for +2 dopants in Cr_2O_3[15, 47] and CeO_2 [14, 39, 40, 42, 46], and for +3 dopants in CeO_2 [43-45] and TiO_2.[35, 36] The removal of a second lattice oxygen to form an oxygen vacancy has an energy requirement and is termed the 'active' or reducing oxygen vacancy.

For undoped bulk chromia, under O-rich/Cr-poor conditions, Cr vacancies (V_{Cr}''') are dominant defects, while under O-poor/Cr-rich conditions O vacancies ($V_O^{\cdot\cdot}$) dominate. When bulk Cr_2O_3

4

is doped with Mg^{2+}, the most stable defect under O-rich/Cr-poor conditions changes to Mg on a Cr lattice site. The formation of holes suggests that p-type behavior should be possible. However, under O-poor conditions the system cannot be doped p-type as O vacancies are expected to compensate and fill the hole states. [14, 48-54] This indicates that vacancy formation, either cation or anion, appears to be the dominant defect that forms in undoped chromia and doping the system can modify the dominant defects formed and change the nature of the conductivity in the systems.

For IVD of chromia, the oxidation state is the same as Cr^{3+} so that there is no change in charge around the substitutional dopant lattice site and the system remains charge balanced with no extra electrons or holes present, as shown;

$$Cr_{Cr}^x + M_2O_3 \rightarrow M_{Cr}^x + Cr_2O_3 \qquad \text{(Charge neutral process)}$$
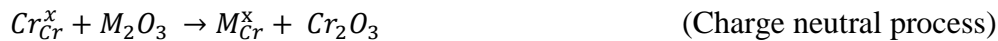
Where M is an IVD that has an oxidation state of +3, and M_{Cr}^x is the metal substituting a Cr^{3+} lattice site with an effective neutral charge. Doping chromia with such dopants will modify the local atomic structure, and the electronic and magnetic properties by altering the magnetic ordering and changing the band gap separation of the valence band maximum (VBM) and conduction band minimum (CBM) as observed for Fe doping of chromia.[55] Although IVDs will not introduce acceptor or donor states, they do alter the material on an electronic level and local geometry that can lead to improved ion conduction and band-gap engineering approaches for more efficient oxygen transport mediums or photo catalysis applications.

The use of IVDs in metal oxides to improve electronic and ionic conductivities for various applications and catalysis is well-known.[56, 57] For example, Ag_2SO_4 is an alkali metal free solid based electrolyte with high cationic conductivity, and doping this material with the IVDs Ca^{2+} and Ba^{2+} greatly improves its conductivity in both α and β phases.[58] The origins of the increased conductivity in the doped systems is attributed to the presence of the dopants that

promote Ag^+ vacancy formation which is also affected by the size of the dopant ionic radius. Isovalent doping of CeO_2 by Zr is found to improve the catalytic performance of ceria towards soot and CO oxidation by promoting oxygen vacancy formation over the undoped structures.[59] The promotion of oxygen vacancy formation is attributed to the local distortions caused by the IVDs and also the changes in the electronic structure which increases the concentration of oxygen vacancies for greater catalytic performance.[60, 61] A range of Frenkel and Schottky-type defects and the effect of isovalent doping on their formation was studied in $MgTa_2O_6$.[62] Substitutional doping of the Mg^{2+} by other M^{2+} dopants was found to improve the ionic conductivity and the redox properties of the material. For materials with similar corundum structures such as Al_2O_3, and Fe_2O_3, isovalent doping has positive effects on the electronic properties of the systems. Al^{3+} surface treatment of Ti doped Fe_2O_3 has a positive effect on the photochemical properties of the material for water splitting applications making it a more efficient photo-catalyst than either Fe_2O_3 or $Ti-Fe_2O_3$.[63] The presence of the isovalent Al^{3+} atom passivates the surface charge by introduction of surface states that improve electron-hole separation, preventing charge recombination. Not only can isovalent doping occur at the cation lattice sites, but substitutional doping of IVDs at the anion sites to improve materials properties can also be examined. Sulfur doping in Fe_2O_3 replaces the O anion site and the presence of S atoms reduce the fundamental band gap of the material which is correlated to the concentration of S doping.[64] Modifying properties of Cr_2O_3 in such a way by IVDs could modify redox properties of the material and the nature of the dominant bulk defects.

Defect chemistry in metal oxides focuses on cation/anion interstitials and vacancies, and Frenkel defects to understand the redox properties of a material for catalytic applications. However a defect that can form in oxides that has received less attention in the current literature is the formation of peroxides (O_2^{2-}). Peroxide defects are typically examined at surfaces of

metal oxides in catalysis as they act as active species to promote surface reactions or photo-catalysis in materials such as TiO_2 which are identified by electron paramagnetic resonance spectroscopy (EPR).[65] Indeed, peroxide formation is found to occur at the surfaces of CeO_2 and crucial to the oxygenation potential of the catalyst for a number of surface reactions and soot prevention.[66-68] Peroxide formation is also suggest to form in the CeO_2 bulk and vital to the OSC potential of the material for SOFC applications and in oxygenation catalysis.[69] The peroxide formation in bulk materials, e.g. in group two binary oxides such as MgO,[70] can act as source of excess oxygen in the metal oxide bulk that can be released under suitable operating conditions to supply oxygen to the surface for catalytic reactions or as an OSC material for SOFC applications. The formation of peroxides to store and release excess oxygen is also seen in ternary oxides such as zirconate perovskites where the peroxide defect greatly promotes anion migration throughout the material to greatly improve its OSC properties.[71] The formation of peroxide defects is not possible for all metal oxides as for example, CeO_2 and ThO_2 cannot accommodate O^{2-} interstitials as their cations cannot be oxidized to a valence state of +5.[72] For metal oxides such as chromium oxide, oxygen interstitials can exist in Cr_2O_3 since Cr can have a +4 valence state and the formation of peroxides as a charge neutral defect has been reported but not examined in detail.[14] Peroxide formation in Cr_2O_3 as a means to enhance the OSC for oxidative catalysis is therefore interesting and requires investigation to determine their role in defect chemistry for Cr_2O_3 and also the effect of IVDs on their formation.

This study uses DFT with Hubbard +U corrections to the Cr 3d states (DFT+U) to assess the effect of isovalent doping on the geometric and electronic structure in bulk chromia. The IS dopants that we will examine are Al, La, and Fe that have the structure M_2O_3 as their most stable structure for their parent oxides. Al and Fe doping in Cr_2O_3 do not distort the structure while the larger La dopant is seen to cause local distortions in the bulk oxide. Al doping does

not greatly change the defect formation energies in Cr_2O_3 while Fe doping is seen to increase the formation energies of oxygen interstitials, Frenkel oxygen defect and peroxide formation while decreasing the oxygen vacancy formation energy. For La doping in Cr_2O_3, the formation energies of Cr vacancies and Cr Frenkel defects are greatly lowered indicating that the presence of La dopants improved the formation of Cr vacancies in Cr_2O_3.

2.   Computational Methodology:

All calculations are carried out using density functional theory (DFT) within the generalised gradient approximation (GGA)[73] using the Perdew-Burke-Ernzerhof (PBE)[74] exchange-correlation functional as implemented in the Vienna Ab initio Simulation Package (VASP).[75-77] The valence electrons are described using a plane wave basis set and the interaction of the core (Cr:[Ar], O:[He], Al:[Ne], Fe:[Ar], La:[Xe]) and valence (Cr $3d^5$ $4s^1$, O $2s^2$ $2p^4$, Al $3s^2$ $3p^1$, Fe $3p^6$ $3d^7$ $4s^1$, La $5p^6$ $5d^1$ $6s^2$) electrons is described using the projector augmented wave method (PAW).[78, 79] The Hubbard +U correction (PBE+U) as described by Dudarev *et al.*[80, 81] for the electronic on-site coulombic interactions is applied to the Cr 3d (+U=5eV) and O 2p (+U = 5.5eV) states which has been shown to correctly described the ground state electronic and magnetic structure of Cr_2O_3 and doped Cr_2O_3.[12, 13, 15] The application of a Hubbard +U correction also been applied to the valence states of dopants that have varying oxidation states, which in this case is Fe 3d (+U = 4.5eV).[12]

The α-Cr_2O_3 bulk is optimised using a conjugated gradient algorithm at a series of constant volume calculations with the atomic positions and lattice vectors being allowed to relax, and the unit cell lattice constant parameter is varied from ±2% of the experimental lattice constant. This was carried out for a number of *k*-point meshes (4x4x4, 6x6x6, 8x8x8) using the Monkhorst-Pack method,[82] and a number of energy

8

cut-off values (400eV, 500eV, 600eV). The obtained energies for each series of k-point meshes and energy cut-offs were fitted to the Murnaghan equation of state[83] to determine the parameters that provided the lowest energy structure for bulk α-Cr_2O_3. This approach is used to avoid the issues associated with Pulay stress that can occur for plane wave calculations. The optimised parameters for the minimum energy $Cr_{12}O_{18}$ bulk were found for a k-point mesh of (4x4x4) and an energy cut-off of 500eV, where the lattice constants a=5.08Å, b=4.40Å and c=13.93Å deviate from the experimental lattice by 2.48%.[84] The structures were deemed converged when the forces on the atoms were reduced to below 0.02 eV/Å.

To accommodate the inclusion of a dopant species of reasonable concentrations, and remove any interactions between images under periodic boundary conditions, the bulk cell for α-Cr_2O_3 was expanded to a 2x2x2 supercell with a $Cr_{96}O_{144}$ composition; this results in a 1.04% doping concentration for one metal atom on a Cr lattice site. This super cell was relaxed at an energy cut off of 500 eV but with a reduced k-point mesh of (2x2x2). One of the Cr cations was replaced on its lattice site with a dopant metal species, and the system was relaxed to obtain the total energies for the doped structures.

The following defects were examined in the undoped Cr_2O_3 structure and each of the doped structures; Cr interstitials and vacancies, O interstitials and vacancies, peroxide formation (O_p) , and Frenkel defects for $[Cr_i^{\cdots} + V_{Cr}''']$, $[O_i'' + V_{\ddot{O}}]$ and $[O_i'' + O_{\ddot{p}}]$. All defects were exhaustively investigated in the undoped and metal (Al, Fe, La) doped structures by examining neighbouring (N), next neighbouring (NN), next next neighbouring (NNN) positions relative to the defect or dopant sites. This gave between 9 and 12 individual configurations (the exact number is symmetry dependent) to test

each defect in each undoped and doped chromia structure. The chromium interstitial formation was investigated by examining different positions of the Cr atom in the Cr and O layers, as well as the interstitial site between layers with the lowest energy configuration formation energy ($E[Cr_i]$) calculated by;

$$E[Cr_i] = E[M_x:Cr_{(2+y)-x}O_3] - (E[M_x:Cr_{(2-x)}O_3] + yE[Cr_m])$$

Where $E[M_x:Cr_{(2+y)-x}O_3]$ is the calculated energy for the metal (M) doped Cr_2O_3 lattice containing the Cr interstitial, $E[M_x:Cr_{(2-x)}O_3]$ is the calculated energy for the M doped lattice and $E[Cr_m]$ is the calculated energy per Cr atom in bulk Cr bcc metal. Chromium vacancy formation is examined by removing a Cr cation from its lattice sites in next nearest and nearest neighbour positions in the lattice relative to the metal with the calculated formation energy given by;

$$E[Cr\ vac] = E[M_x:Cr_{(2-y)-x}O_3] + yE[Cr_m] - E[M_x:Cr_{(2-x)}O_3]$$

$E[M_x:Cr_{(2-y)-x}O_3]$ is the calculated energy for the Cr vacancy in the M doped Cr_2O_3 lattice. The oxygen interstitial formation is examined in a similar manner to Cr interstitial formation and the formation energy ($E[O_i]$) is calculated by;

$$E[O_i] = E[M_x:Cr_{(2-x)}O_{(3+y)}] - (E[M_x:Cr_{(2-x)}O_3] + y/2\ E[O_2])$$

$E[M_x:Cr_{(2-x)}O_{(3+y)}]$ is the calculated energy for the M doped Cr_2O_3 lattice with an O interstitial and $E[O_2]$ is the calculated energy for gaseous O_2 in a vacuum with a Hubbard +U correction (+U = 5.5eV) applied to the O 2p states. The formation energy of a peroxide defect (O_p) can be calculated in a similar manner, as an oxygen atom is added to the bulk bound to a lattice oxygen site. The oxygen vacancy formation was investigated by exploring the removal of a lattice oxygen species from next nearest and

next-next nearest neighbour sites to the metal dopant atom. The formation energy of each vacancy was calculated by;

$$E[Ovac] = (E[M_x\text{-}Cr_{(2\text{-}x)}O_{(3\text{-}y)}] + \tfrac{1}{2} E[O_2]) - E[M_x\text{-}Cr_{(2\text{-}x)}O_3]$$

Where $E[M_x\text{-}Cr_{(2\text{-}x)}O_{(3\text{-}y)}]$ is the calculated energy for the metal (M) doped bulk α-Cr_2O_3 with an oxygen vacancy, $E[O_2]$ is the calculated energy of gaseous O_2 and $E[M_x\text{-}Cr_{(2\text{-}x)}O_3]$ is the calculated energy for bulk M doped α-Cr_2O_3.

Frenkel defects are linked to the redox potential of the material and can be calculated by exploring the formation of Cr/O interstitials/vacancies at different positions nearest neighbour or next nearest neighbour to each other in the bulk lattice. For the doped systems this becomes complex as the dopant cation breaks the bulk symmetry and both interstitials/vacancies are varied to determine low energy arrangement in the lattice which does not necessarily correspond to the most favoured positions of the individual point defects. The formation energy for the Cr (E[Cr Fren]) and O (E[O Fren]) Frenkel defects is calculated by;

$$E[Cr\ Fren] = E[Cr_i^{\cdots} + V_{Cr}'''] - E[M_x\text{:}Cr_{(2\text{-}x)}O_3]$$

$$E[O\ Fren] = E[O_i'' + V_{\ddot{O}}] - E[M_x\text{:}Cr_{(2\text{-}x)}O_3]$$

Where $E[Cr_i^{\cdots} + V_{Cr}''']$ is the calculated energy for the Cr interstitial and Cr vacancy, and $E[O_i'' + V_{\ddot{O}}]$ is the calculated energy for the O interstitial and O vacancy in the M doped Cr_2O_3 bulk. Schottky defect formation is also investigated by removing oxygen anions and examining subsequent removal of neighbouring Cr cations to determine the lowest energy distribution of Cr and O vacancies. The formation energy is calculated by;

$$E[Schottky] = E[2V_{Cr}''' + 3V_{\ddot{O}}] - E[Cr_2O_3]$$

Where $E[2V'''_{Cr} + 3V^{\cdot\cdot}_{O}]$ is the calculated energy of the Cr$_2$O$_3$ lattice containing two Cr vacancies and three O vacancies to charge balance the bulk.

In the present study we limit our focus to the effect of isovalent doping on the formation of neutral defects without any applied bias. Investigating charge states in the doped chromia systems in this paper is computationally challenging for the multiple dopants in this study and is beyond the scope of the present paper.

The electronic structure for each of the systems under consideration are examined using the partial (ion and quantum number l decomposed) electronic density of states (PEDOS). The charge interactions and transfer processes are investigated using Bader's atoms in molecules (AIM) approach as implemented in VASP by the Henkleman group,[85-88] and computed spin magnetisations.

3.   Results:

Point, Frenkel and Schottky defects in bulk chromia

The calculated structure for bulk α-Cr$_2$O$_3$ and the PEDOS are shown in Figure 1(a) and (b). The Cr^{3+} cations adopt a distorted octahedral environment in the bulk lattice, while the O^{2-} anions have a tetrahedral geometry. The structure of the bulk Chromia is composed of alternating, neutral stoichiometric Cr$_4$O$_6$ layers and the calculated Cr-O bond lengths range from 2.02Å to 2.05Å. The calculated PEDOS plot for bulk Chromia shows that the valence band (VB) and conduction band (CB) are a mixture of Cr 3d and O 2p states. The VB has similar degrees of mixing from the two species while the CB is dominated by Cr 3d states. The calculated band gap between the VB maximum (VBM) and CB minimum (CBM) is 2.60 eV which is underestimated from the experimental value but within the reported range for PBE+U

calculations.[9, 14] The Cr cations and O anions have computed Bader charges of 4.0 and 7.0 electrons respectively.
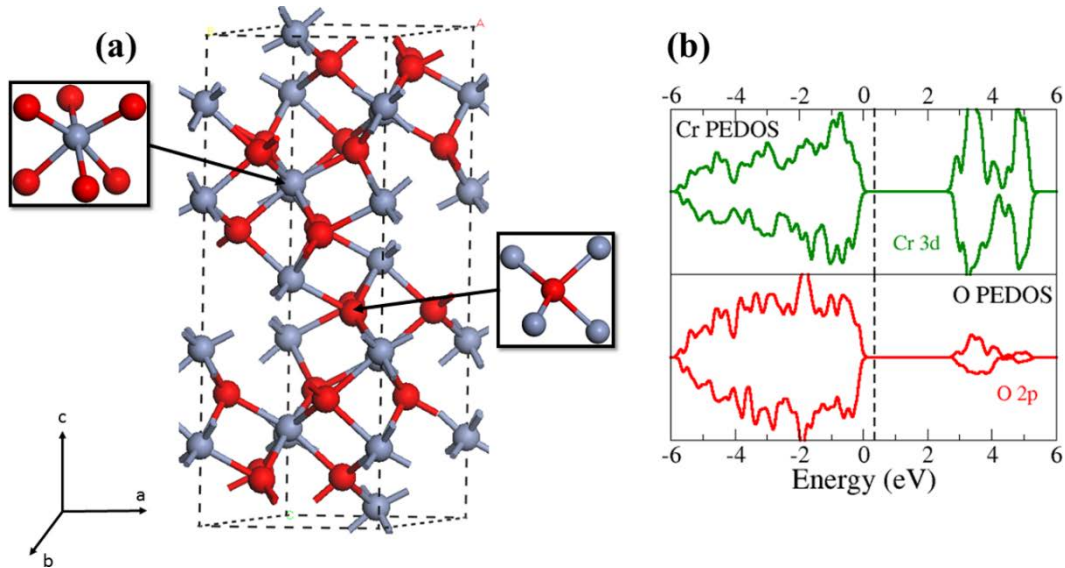

Figure 1: The calculated bulk structure of chromia and corresponding PEDOS plots. The grey, and red spheres are the lattice positions of the Cr^{3+} and O^{2-} atoms. The green and red lines are the Cr 3d and O 2p states in the PEDOS, while the top of the valence band is set to 0eV and the dotted line is the Fermi level.

The point defects that are considered in the bulk Cr_2O_3 lattice are; Cr interstitial and vacancy, O interstitial and vacancy, and peroxide formation. The calculated formation energies for each of the point defects are given in Table 1 and show that the oxygen related defects have lower formation energies than the Cr defects, and the lowest energy is associated with peroxide formation. The values show that O vacancies and interstitials are more dominant than Cr point defects; however any oxygen atoms that are introduced into the bulk are more likely to form peroxides with lattice oxygen than reside in interstitial sites.

Table 1: The calculated formation energies for various point defects in bulk Cr_2O_3.

	E_f (eV)
O vacancy	4.11
Cr vacancy	4.59
O interstitial	3.60
Cr interstitial	5.46
Peroxide	2.52

The lowest energy arrangement for each of the point defects and their corresponding PEDOS plots are given in Figure 2 and the calculated formation energies for these structures of each defect are given in Table 1. The formation of an oxygen vacancy releases two electrons into the lattice which partially reduce four neighbouring Cr cations in the Cr layers above and below the vacancy position. Attempts to localise the electrons on two neighbour proved unsuccessful as all calculations resulted in a configuration to that shown in Figure 2(a). The reduced Cr cations are identified by Bader analysis and spin magnetisation values. The Cr cations are reduced from Cr^{3+} to $Cr^{(3-\delta)}$ with an increase in computed Bader charges from 4.0 electrons (e^-) to 4.3 e^- and spin magnetisations of 3.3 spins (3.0 spins in stoichiometric Cr_2O_3). The partially reduced Cr cations have opposing spins giving an overall singlet spin configuration. The PEDOS plot for the oxygen vacancy shows that the formation of an O vacancy creates an occupied Cr defect peak around 1 eV and an unoccupied Cr peak around 2 eV above the top of the valence band. Both Cr atoms ($Cr_1 + Cr_2$) in the layer above the O vacancy contribute to the α-spin of these peaks, while the Cr atoms in the layer below the O vacancy contribute to the β-spin. For the Cr vacancy, three holes are found on the neighbouring lattice O species forming three O^- atoms, one above the Cr vacancy and two below the vacancy. The Bader charges for these O species are reduced from 7.3 e^- to 7.0 e^- and they have a spin magnetisation value of

14

0.7 spins, typical of oxygen polarons. The formation of hole states on each of the O species is shown in the PEDOS as the three unoccupied O 2p peaks found above the Fermi level in the band gap from 0.9 - 1.2 eV above the top of the valence band. The overall spin for the Cr vacancy is 3.

The preferential site for the **oxygen interstitial** was found to be an interstitial site in the Cr layer where the O_i is bonded to one Cr atom in each layer, with Cr-O bond lengths of 2.09Å (x2) as shown in Figure 2(c). The oxygen interstitial is an O^- species with a computed Bader charge of 6.48 e^- and a spin of 1.17 spins with no indication of reduction/oxidation to any surrounding atoms. The O interstitial introduces an occupied O 2p defect peak into the band gap around 0.5eV above the top of the valence band as shown in the calculated PEDOS plot.

The **Cr interstitial** (Figure 2(d)) preferentially lies in the interstitial site in the Cr layer in a square planar configuration bonding to two oxygen atoms above and two oxygen atoms below with Cr-O distances of 2.03Å (x2) and 2.13Å (x2) with an overall system spin of 4. Three Cr cations are reduced by the presence of the Cr_i from Cr^{3+} to Cr^{2+} with an increase in their Bader charges from 4.0 e^- to 4.5 e^- and a spin magnetisation of 3.5 spins. Two of the reduce Cr cations are located next nearest neighbour from the Cr interstitial and one is located in the layer below. The reduction of the Cr cations introduces Cr defect peaks between 0 – 0.9 eV and 1.55 – 2.0 eV in the band gap from the top of the valence band.

The **peroxide formation** in the Cr_2O_3 lattice is shown in Figure 2(e) when the introduced O^{2-} species bonds to a lattice oxygen atom forming O_2^{2-}. The lattice oxygen changes its geometry to facilitate the formation of the peroxide with both O atoms adopting bridging positions in the O layer between two Cr layers with four calculated Cr-O bonds of 2.03Å (x2) and 2.00Å (x2), and also forming an O-O bond of 1.48Å which is typical of peroxide formation.[65] The Bader

charge for the lattice oxygen reduces from 7.3 e⁻ to 6.7 e⁻ and the Bader charge of the O atom

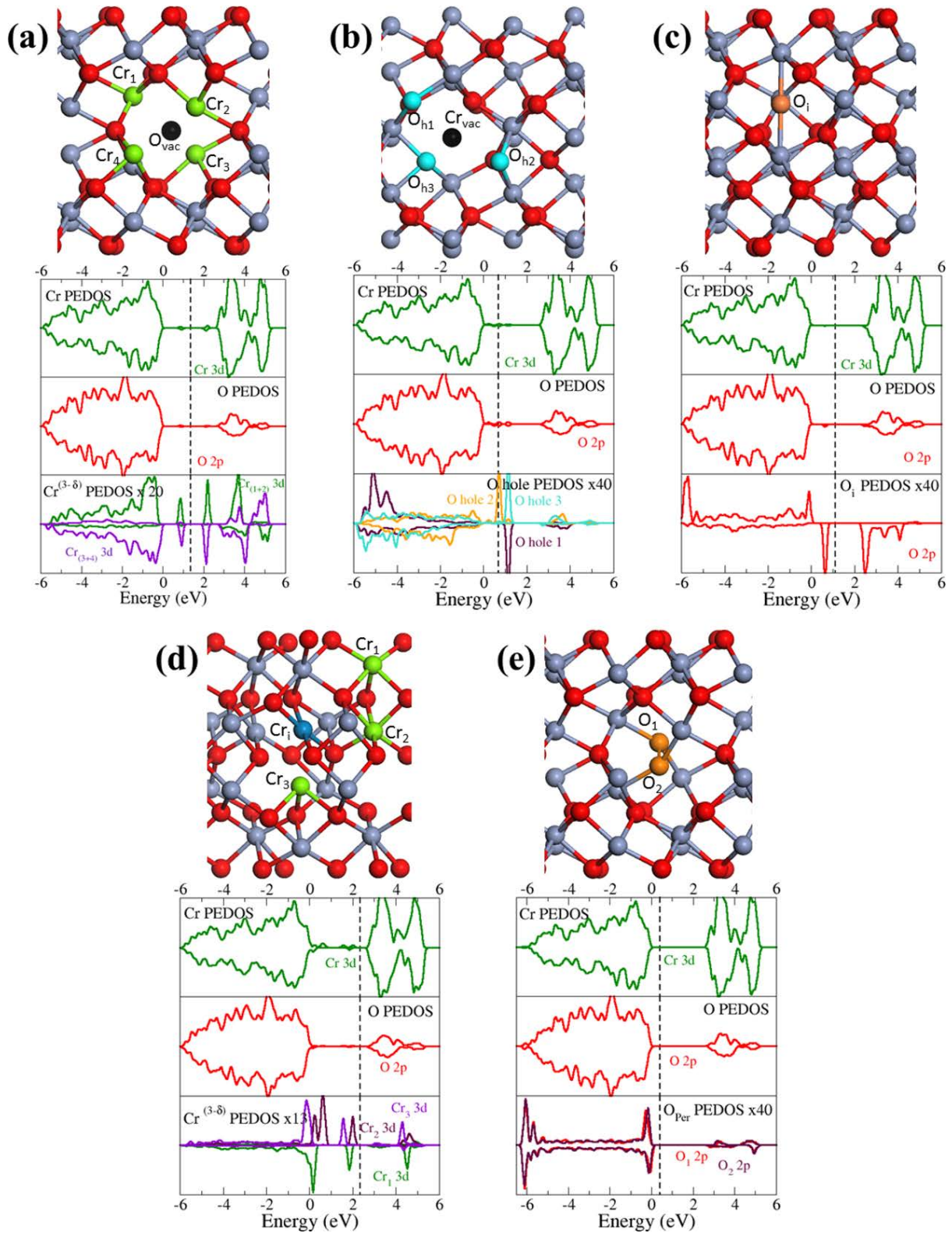forming the bond with the lattice oxygen is 6.7 e⁻. Both atoms have a spin of 0.

Figure 2: The calculated local geometry and PEDOS plots for (a) Oxygen vacancy, (b) Cr vacancy, (c) Oxygen interstitial, (d) Cr interstitial and (e) peroxide formation. The grey and red spheres are the lattice Cr and O atoms,

while the green atoms are the reduce Cr cations, the light blue atoms are the oxidised O anions, the orange atom is the O interstitial and the peroxide, and the dark blue atom is the Cr interstitial. The green and red lines in the PEDOS plot are the Cr 3d and O 2p states, while the lower panels show the defect states. The top of the valence band is aligned to 0ev in all plots and the Fermi level is indicated by the dotted line.

The calculated formation energies for the lowest energy configurations of the **Frenkel and Schottky defects** in bulk Cr_2O_3 are given in Table 2. The pairing of Cr vacancy and Cr interstitial is considerably more favourable than the other Frenkel defects and, in particular, the Schottky defect. The high formation energy for Schottky defects indicates that these are the least likely defect to occur in Cr_2O_3 and will not be investigated for the doped systems. The lower formation energy of the Cr Frenkel defect indicates that this defect pairing will dominate over formation of the oxygen and peroxide Frenkel defects which has also been seen by other DFT studies.[9] However the peroxide formation energy is similar to the Cr Frenkel defect formation energy indicating that these could be competing process in the Cr_2O_3 bulk which has not been shown previously.

Table 2: The calculated formation energies for the Cr, O, Peroxide Frenkel defects and the Schottky defect.

	E[f] eV
Cr Frenkel pair	2.33
O Frenkel pair	6.75
Peroxide Frenkel pair	6.64
Schottky defect	10.72

The calculated lowest energy configuration for the formation of **Cr and O Frenkel defects** are shown in Figure 3(a) and (b), with a Frenkel-type defect combination of an O vacancy and peroxide shown in Figure 3(c). A Schottky defect in bulk Cr_2O_3 is also shown in Figure 3(d). For the Cr Frenkel defect, the Cr interstitial is located nearest neighbour to the Cr vacancy in the O layer below, and it changes its geometry from the four fold square planar to a three-fold

trigonal pyramidal geometry with Cr-O bonds of 1.95Å (x3). The Cr interstitial moves to lie half way between the vacancy and previous interstitial site to compensate for the vacancy. The overall defect has a neutral charge as the three holes on neighbouring O atoms are filled by the electron donating Cr interstitial. The Bader charges for these O atoms have increased from 7.0 to 7.3 e$^-$ and have a spin magnetisation of 0. The filling of the holes is also seen in the PEDOS plots as the lower panel shows that the previously unoccupied O 2p states above the Fermi level are now filled and located in the band gap around 1eV from the top of the valence band. The PEDOS plot for the Cr interstitial shows no occupied defect peaks and shows an unoccupied Cr 3d peak around 2.0eV.

For the oxygen Frenkel defect, the oxygen interstitial is located in the nearest neighbour interstitial site to the oxygen vacancy. The oxygen vacancy reduces two neighbouring Cr cations, confirmed by an increase in their computed Bader charges from 4.0 to 4.5 e$^-$ and each have a spin magnetisation of 3.5 electrons in a singlet configuration. The O interstitial remains as O$^-$ with a Bader charge of 6.5 e$^-$ and a spin magnetisation value of 1.15. There are no oxidised species in the system to compensate for the reduced Cr cations, so that the oxygen Frenkel defect is not charge balanced, and hence a high formation energy. The PEDOS plots for the reduced Cr cations show that occupied Cr 3d defect peaks are located around 1eV above the top of the valence band and the O interstitial has an occupied O 2p peak in the band gap at a similar energy. The Frenkel defect combination for oxygen vacancy and peroxide shows that the peroxide forms nearest neighbour to the vacancy. The oxygen vacancy reduces two neighbouring Cr cations, confirmed by the change in Bader charge from 4.0 to 4.5 e$^-$ and the peroxide has Bader charge of 6.7 e$^-$ for both O atoms. The overall system spin is 0 as the reduced Cr cations have opposing spins and the peroxide has no spin. The PEDOS plot shows that the reduced Cr cations introduce an occupied Cr 3d defect peak around 1eV above the top of the valence band, while the peroxide introduces no defect states.

The lowest energy configuration for the Schottky defect shows that the cation and anion vacancies preferentially form next neighbour to each other in a cluster of vacancies in the bulk lattice. The Cr vacancies (yellow spheres) form in the same layer while the oxygen vacancies (black spheres) are distributed between the oxygen layer above and below the Cr layer. Although both vacancy formations compensate each other so that electrons release from the O vacancies fill the holes (O^-) formed from Cr vacancies, the overall system spin is 6 since the magnetic ordering in the alternating Cr layers is disturbed having unpaired electrons from the absence of cations and anions. The PEDOS plots shows that there are no defect peaks in the band gap since the holes are compensated by the electrons.
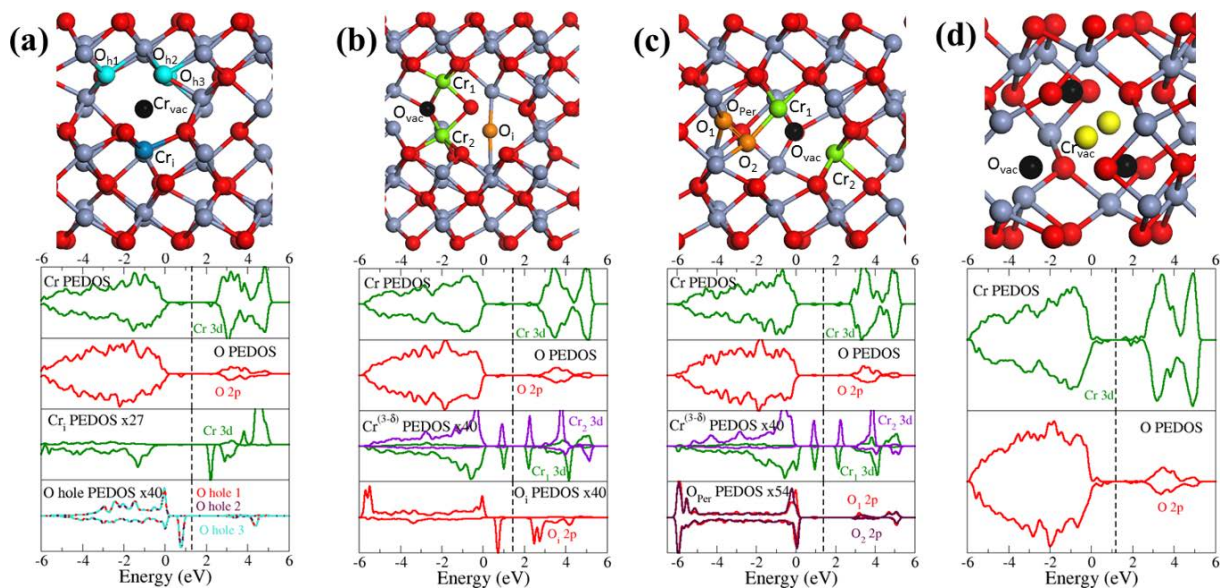

Figure 3: The calculated local geometry and PEDOS plots for (a) Cr Frenkel, (b) O Frenkel, (c) Peroxide Frenkel, and (d) Schottky defects. The grey and red spheres are the lattice Cr and O atoms, while the green atoms are the reduce Cr cations, the light blue atoms are the oxidised O anions, the orange atom is the O interstitial and the peroxide, and the dark blue atom is the Cr interstitial. The black spheres are the vacancies and in the case of the Schottky defect, the yellow spheres are the Cr vacancies. The green and red lines in the PEDOS plot are the Cr 3d and O 2p states, while the lower panels show the defect states. The top of the valence band is aligned to 0ev in all plots and the Fermi level is indicated by the dotted line.

Isovalent doping in bulk Cr_2O_3

Metal doped Cr_2O_3 structures

The doping of bulk Cr_2O_3 was carried out by substitutionally replacing Cr^{3+} cations on their lattice site with Al^{3+}, Fe^{3+} and La^{3+} cations. The calculated local geometry around the dopant cation in bulk Cr_2O_3 is shown in Figure 4, along with the corresponding calculated PEDOS plots. The Al dopant relaxes from the octahedral geometry of the Cr^{3+} cation to a three-fold trigonal planar geometry with Al-O bonds of 1.91Å (x3) which are shorter than Cr-O bonds, causing local distortions around the Al dopant. The PEDOS plot shows that the Al dopant does not introduce any defect states into the band gap, and has a negligible contribution of Al 3s/p states to the VB and to the CB. The calculated band gap between the VB and CB is 2.72eV which is a small increase on the calculated fundamental band gap for undoped Cr_2O_3 (2.60eV). The Bader charge for the Al atom is 0 e⁻ confirming that it has a +3 oxidation state and no other species in the bulk are reduced/oxidised.

For Fe doping in Cr_2O_3, the Fe dopant maintains the octahedral geometry similar to the Cr geometry with calculated Fe-O bonds of 1.98Å (x3) with the O layer below the dopant, and bond lengths of 2.01Å (x3) with the O layer above the dopant. The calculated PEDOS plot shows that the VB and CB are a mixture of Fe 3d states with Cr 3d and O 2p states. The Fe 3d states have an occupied β spin peak that lies above the top of the Cr and O states, while there is an unoccupied Fe 3d peak at the bottom of the CB below the Cr and O states. The calculated fundamental band gap between the VBM and CBM is 2.12eV which is a decrease compared to

the undoped Cr_2O_3 band gap. The Fe dopant has a Bader charge of 12.4 e$^-$ and prefers to have a high spin magnetisation of 4.26 spins.

The La dopant in Cr_2O_3 maintains the six coordination around the cation but changes to a distorted trigonal prism geometry with La-O bond lengths of 2.48Å (x3) to the O layer above the dopant cation, and 2.23Å (x3) to the O layer below the dopant cation. The PEDOS plots show that, similar to Al, the La 5 p/d and 6s states have negligible contributions to the VB and CB. The La dopant has a computed Bader charge of 6.8 e$^-$, and a spin magnetisation of 0 spins.
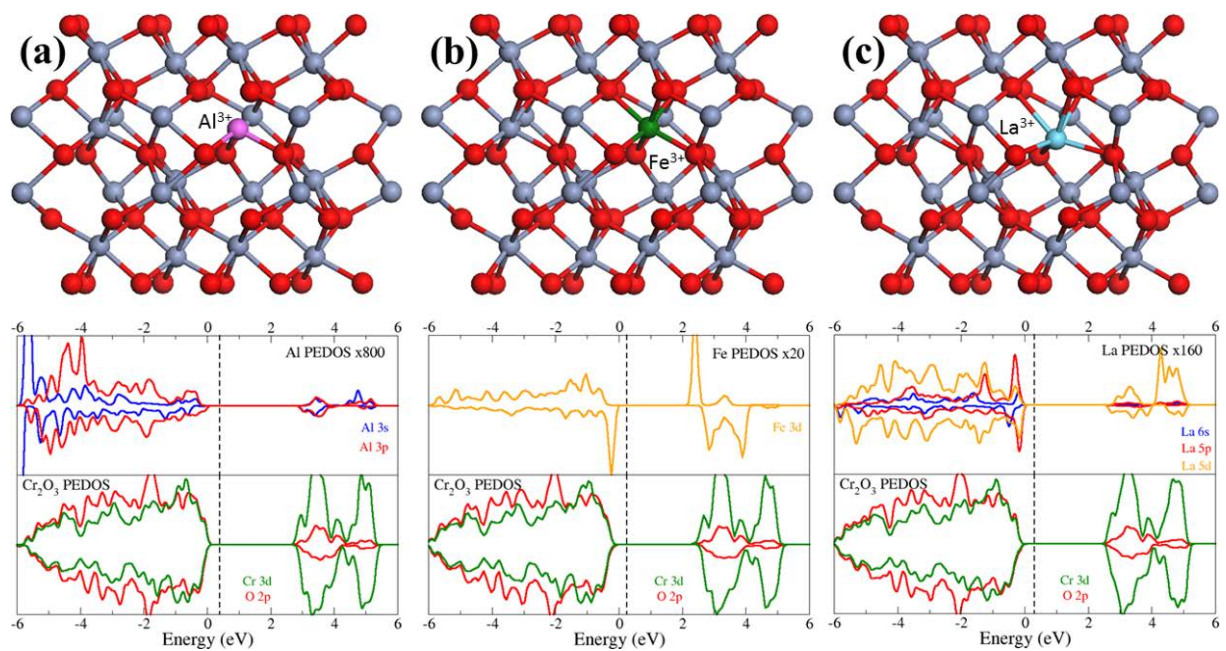

Figure 4: The calculated local geometry and PEDOS plots for (a) Al, (b) Fe, and (c) La doped Cr_2O_3. The grey and red spheres are the lattice Cr and O atoms, while the pink, dark green and light blue atoms are the lattice positions of the Al, Fe and La dopants. The green and orange lines are the Cr and Fe/La d states, while the blue and red lines are the s and p states. The top of the valence band is aligned to 0ev in all plots and the Fermi level is indicated by the dotted line.

Oxygen vacancy, interstitial and peroxide formation in metal doped Cr_2O_3

The calculated formation energies for the most stable oxygen vacancy, oxygen interstitial and peroxide species in undoped and metal doped Cr_2O_3 are given in Table 3. Al doping of Cr_2O_3

21

does not significantly change the formation energies for oxygen vacancy and peroxide over the undoped Cr_2O_3 but it does increase the formation energy of the oxygen interstitial. This may facilitate the formation of peroxide defects which is as favourable as the undoped Cr_2O_3, as any excess oxygen in the lattice will be preferentially incorporated as peroxides. For Fe-Cr_2O_3, the dopant enhances the oxygen vacancy formation and is itself reduced, which is an indicator for improved reducibility and strongly inhibits oxygen interstitial and peroxide formation. Their formation energies are significantly increased because the Fe dopant does not take a +4 oxidation state.

For La-Cr_2O_3, oxygen vacancy and peroxide formation are improved over undoped Cr_2O_3, while the oxygen interstitial is less favourable. The enhancement in oxygen vacancy formation energy arises from the larger ionic radius of La (1.03Å) compared to Cr (0.62Å) which induces local distortions that facilitate oxygen vacancy formation. These distortions also enhance formation of the peroxide and impede oxygen interstitial formation.

Table 3: The calculated formation energies for an oxygen vacancy, an oxygen interstitial and a peroxide in Al, Fe and La doped Cr_2O_3

	E_f [Ovac] (eV)	E_f [O_i] (eV)	E_f [O_p] (eV)
Cr_2O_3	4.11	3.60	2.52
Al-Cr_2O_3	4.01	3.95	2.51
Fe-Cr_2O_3	3.97	6.57	4.08
La-Cr_2O_3	3.83	4.24	2.13

The calculated local structures and PEDOS plots for the oxygen vacancy, oxygen interstitial and peroxide defects are shown in Figure 5 (a), (b) and (c) respectively for in each of the doped structures. For all doped structures, oxygen vacancies preferentially form nearest neighbour to

the dopant cation and release two electrons to reduce neighbouring cations. The reduction process in Al-Cr_2O_3 and La-Cr_2O_3 are similar, reducing two neighbouring Cr cations from Cr^{3+} to Cr^{2+}; the Bader charges change from 4.0 e^- to 4.5 e^- and the spin magnetisation is 3.7 spins for each reduced cation. The reduction of the Cr cations is reflected in the PEDOS for both doped systems with the appearance of a Cr 3d defect peak in the band gap around 1eV from the VBM. In Fe-Cr_2O_3 the reduction process is different, the oxygen vacancy reduces one neighbouring Cr cation and the Fe dopant. The reduced Cr^{2+} cation has a Bader charge of 4.5 e^-, and a spin magnetisation of 3.7 spins, and the reduced Fe^{2+} dopant has a Bader charge of 12.7 e^-. The spin magnetisation of the Fe dopant changes from 4.26 spins to 3.70 spins arising from Fe reduction and spin paring of two electrons. The reduction of the Cr and Fe cations is shown in the PEDOS plot as Cr and Fe 3d occupied defect peaks now appear in the band gap at 0.65 to 1.46eV, respectively, from the top of the VB.

Oxygen vacancy formation in Al-Cr_2O_3, Figure 5(a)(i), changes the Al coordination to a distorted five-fold trigonal bipyramidal geometry with Al-O bond lengths of 1.96Å (x2) to the O layer above the dopant, and 1.92Å, 1.89Å, and 1.80Å to the O layer below the dopant. The oxygen vacancy forms nearest neighbour to the La dopant in La-Cr_2O_3 (Figure 5(a)(iii)), with the La dopant maintaining its initial geometry, but with the loss of one bond from the O vacancy. The La-O bonds are similar to the doped bulk. The formation of an oxygen vacancy in Fe-Cr_2O_3 (Figure 5(a)(ii)) removes an oxygen atom previously bound to Fe and changes the coordination of the Fe cation to a five-fold configuration with Fe-O bond lengths of 2.15Å (x3) to the O layer above the dopant and 2.05Å, 2.00Å to the O layer below the dopant.

The preferential positions for oxygen interstitial (Figure 5(b)) are next nearest neighbour to the Al dopant in the Cr layer above Al, but in the same Cr layer as the dopant in both Fe-Cr_2O_3 and La-Cr_2O_3. All bonding geometries and oxidation states for the dopant cations are unaffected by the presence of the interstitial in the bulk, and the oxygen interstitial has a computed Bader

charge of 6.3 e$^-$ indicating it is O$^-$, with no cation reduction or oxidation. The PEDOS plots for each doped lattice indicate that the O interstitial introduces an occupied O 2p defect peak around 0.5eV above the top of the VB.

Regarding peroxide formation, for each dopant the bonding and oxidation states of the dopants remain similar to the doped lattices (Figure 4), while the dopant-oxygen bond lengths are also similar indicating that the peroxide only affects the local structure. The position of the peroxide relative to the dopant is next next nearest neighbour above the Al dopant, nearest neighbour in Fe-Cr$_2$O$_3$ and next nearest neighbour below the La dopant. In each case the peroxide defect has an O-O bond length of 1.48Å and Cr-O bond lengths ranging from 2.00 – 2.02Å where the O atoms have a bridging geometry between the Cr layers. The O atoms in the peroxide defect each have Bader charges of 6.7 e$^-$ in all structures. As the peroxide has different bonding environment in each of the doped structures, the PEDOS plots show different O 2p overlaps and peaks to the VB and CB; however there are no new defect peaks present in the band gap for any of the doped lattices.
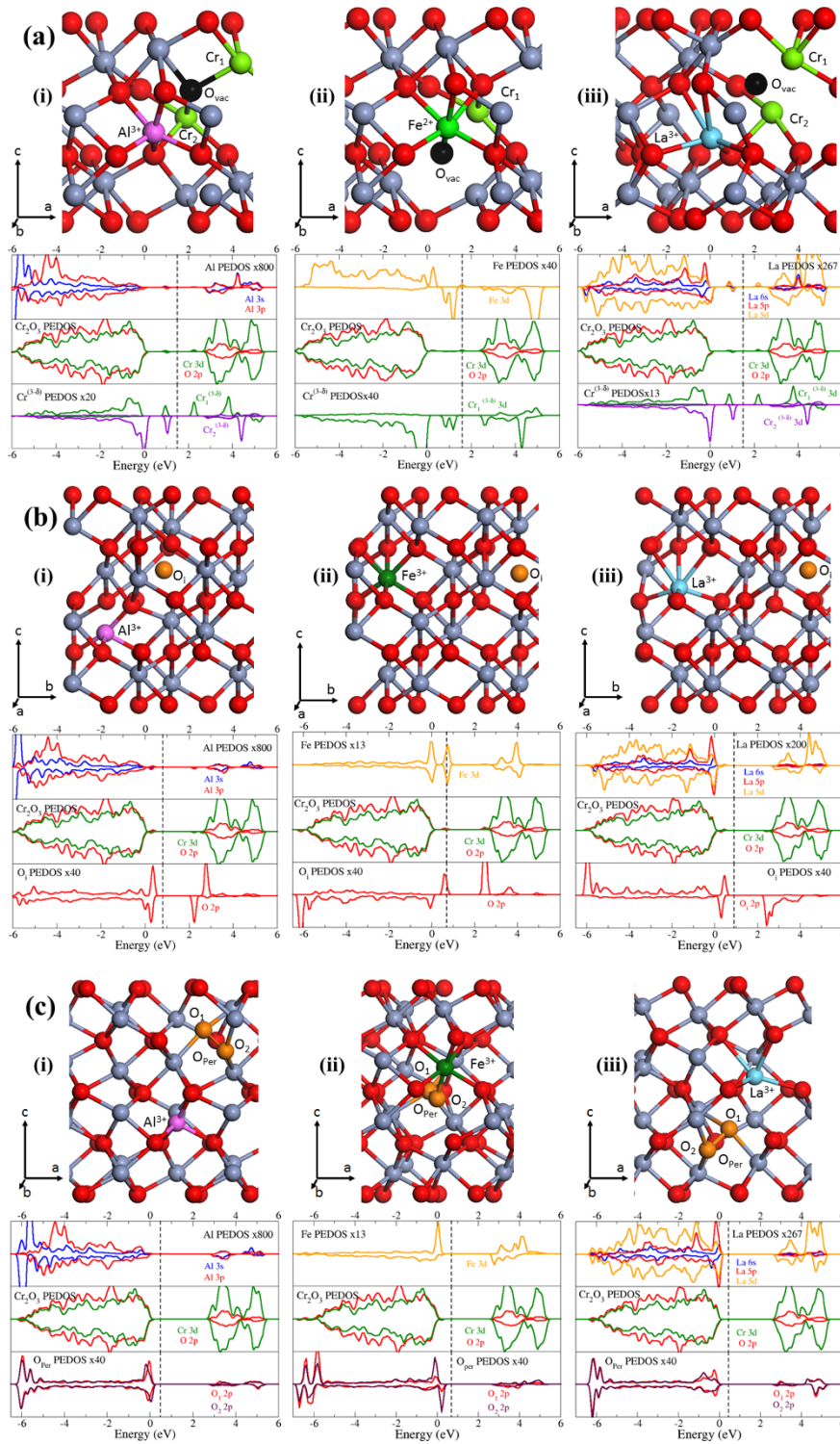
Figure 5: The calculated local geometry and PEDOS plots for (a) oxygen vacancy, (b) oxygen interstitial and (c) peroxide formation in (i) Al-Cr_2O_3, (ii) Fe-Cr_2O_3 and (iii) La-Cr_2O_3. The grey and red spheres are the lattice Cr and O atoms, while the pink, dark green and light blue atoms are the lattice positions of the Al, Fe and La dopants. The black, light green and orange spheres are the lattice positions of the vacancy, reduced Cr and interstitial/peroxide atoms. The green and orange lines are the Cr and Fe/La d states, while the blue and red lines are the s and p states. The top of the valence band is aligned to 0ev in all plots and the Fermi level is indicated by the dotted line.

Chromium vacancy and interstitial formation in metal doped Cr_2O_3

The calculated formation energies for the lowest energy configuration of the Cr vacancy and interstitial in each of the doped structures are given in Table 4, along with the corresponding energies for undoped Cr_2O_3. Al doping in Cr_2O_3 does not significantly affect the formation energies of Cr vacancies and interstitials; the differences are smaller than 0.2 eV. For Fe-Cr_2O_3, formation energies for Cr vacancy and interstitial are greatly increased compared to the undoped lattice, so that Fe doping impedes the formation of Cr vacancies and interstitials. However the opposite is seen for La-Cr_2O_3, as La doping reduces the formation energy of Cr vacancies in Cr_2O_3 while maintaining a similar formation energy for Cr interstitials to the undoped Cr_2O_3 bulk.

Table 4: The calculated formation energies for Cr vacancy and interstitial in Al, Fe and La doped Cr_2O_3.

	E_f [Cr vac] (eV)	E_f [Cr_i] (eV)
Cr_2O_3	4.59	5.46
Al-Cr_2O_3	4.37	5.57
Fe-Cr_2O_3	5.59	6.02
La-Cr_2O_3	3.70	5.36

The lowest energy configuration and PEDOS plots for Cr vacancies and interstitials in Al, Fe and La doped Cr_2O_3 are shown in Figure 6(a) and (b). The Cr vacancy in each of the doped systems is preferentially located next to the dopant cations; in the Cr layer below the Al dopant and in the same Cr layer as the Fe and La dopants. In each case the oxidation state and geometry of the dopant is unaffected by the presence of the Cr vacancy. The Cr vacancy forms three oxygen hole states on O species that were previously bound to the Cr cation as shown in Figure 6 by the light blue atoms. The Bader charges for these O$^-$ species decrease from 7.3 e$^-$ to 7.0 e$^-$

with each O^- atom having a magnetisation of 0.7 spins. The formation of holes on the O anions is reflected in each of the PEDOS plots with the appearance of unoccupied O 2p defect peaks above the fermi level around 1eV from the top of the VB, characteristic of each O^- species.

The Cr interstitial preferentially forms in the next next neighbour position from the Al dopant (Figure 6(b)(i)), in the Cr layer below the Fe dopant in $Fe-Cr_2O_3$ (Figure 6(b)(ii)) and nearest neighbour in the same Cr layer as the La dopant (Figure 6(b)(iii)). In each case the Cr interstitial adopts a four coordinated square planar geometry in the Cr layer binding to two O atoms in each neighbouring oxygen layer with Cr-O bond lengths of 2.11Å and 2.06Å (x3) which are slightly longer than typical Cr-O distances (2.02Å). The formation of a Cr interstitial is a reduction process introducing three extra electrons (Cr_i''') into the bulk lattice which shows similar characteristics in Al and La doped Cr_2O_3. The Cr interstitial reduces two lattice Cr^{3+} cations to Cr^{2+} and is also a Cr^{2+} cation, having computed Bader charges of 4.5 e^-, and a calculated magnetic spin of 3.7 spins. The reduction of Cr cations is reflected in the PEDOS plot as occupied Cr 3d peaks appear in the band gap around 0.5eV and 1.8 – 2.1eV from the top of the VB. The PEDOS plot for the Cr interstitial is consistent with reduced Cr^{2+} cations. For the $Fe-Cr_2O_3$ system, the Cr interstitial reduces a lattice Cr^{3+} cation and the Fe^{3+} dopant to Cr^{2+} and Fe^{2+} with respective Bader charges of 4.5 e^- and 12.8 e^- for Cr^{2+} and Fe^{2+}. The Cr interstitial has an oxidation state of +2 with a computed Bader charge of 4.5 e^- and a spin magnetisation of 0. The PEDOS plot reflects the reduction process as occupied Cr/Fe 3d peaks appear in the band gap around 0 – 1eV and 1.8 – 2.1eV from the reduced Fe/Cr cation and the Cr interstitial cation.
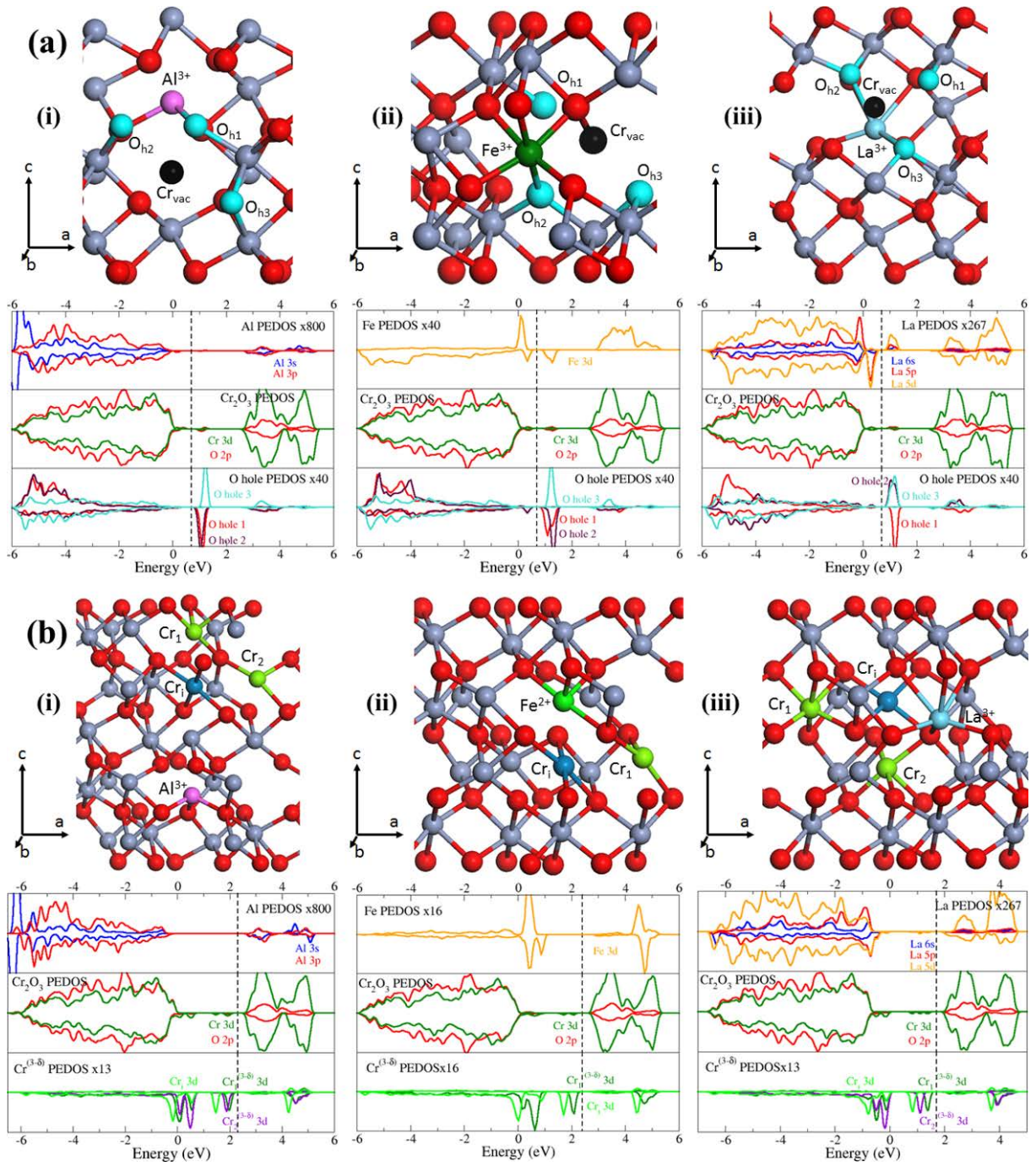
Figure 6: The calculated local geometry and PEDOS plots for (a) Cr vacancy, and (b) Cr interstitial formation in (i) Al-Cr_2O_3, (ii) Fe-Cr_2O_3 and (iii) La-Cr_2O_3. The grey and red spheres are the lattice Cr and O atoms, while the pink, dark green and light blue atoms are the lattice positions of the Al, Fe and La dopants. The black, light green and dark blue spheres are the lattice positions of the Cr vacancy, reduced Cr and Cr interstitial atoms. The green and orange lines are the Cr and Fe/La d states, while the blue and red lines are the s and p states. The top of the valence band is aligned to 0ev in all plots and the Fermi level is indicated by the dotted line.

Chromium, oxygen and peroxide Frenkel defects in metal doped Cr_2O_3

The calculated formation energies for the lowest energy configuration of the Cr, O and peroxide Frenkel defect pairs are given in Table 5. For the Cr Frenkel defect pairing, the Al and Fe dopants do not significantly alter the formation energies while the La dopant reduces the formation energy of the Cr Frenkel defect pair, promoting its formation in Cr_2O_3, this arises from the presence of the large La cation. The Al and Fe dopants greatly increase the formation energies of the O Frenkel pairs compared to undoped Cr_2O_3 and thus suppressing their formation in Cr_2O_3. The formation energy for the peroxide Frenkel pair is relatively unaffected by Al doping, while La enhances the formation, albeit with a larger formation energy and Fe doping greatly increases the defect formation energy. The Cr Frenkel defect is more likely to occur in doped Cr_2O_3 than the other Frenkel defects.

Table 5: The calculated formation energies for Cr, O and Peroxide Frenkel defect pairs in Al, Fe and La doped Cr_2O_3.

	E_f [Cr Fren] (eV)	E_f [O Fren] (eV)	E_f [O_{per} Fren] (eV)
Cr_2O_3	2.34	6.75	6.64
Al-Cr_2O_3	2.17	7.41	6.35
Fe-Cr_2O_3	2.24	8.96	7.79
La-Cr_2O_3	1.32	---	5.22

The calculated local geometry and associated PEDOS plots for the formation of chromium, oxygen and peroxide Frenkel defects in Al, Fe and La doped Cr_2O_3 are shown in Figure 7. For all doped structures, the relative positions of the Cr vacancy and interstitial are nearest neighbour to each other, where the Cr interstitial is positioned between an interstitial site in the Cr layer and the Cr vacancy site. The Cr interstitial has a three-fold trigonal planar geometry

with Cr-O bond distances of 1.95Å (x3) in both Al-Cr$_2$O$_3$ and Fe-Cr$_2$O$_3$ while in La-Cr$_2$O$_3$ it has a five coordinated distorted trigonal bipyramidal geometry with Cr-O bond distances of 1.98Å (x3) and 2.09Å (x2). The position of the Cr Frenkel defect pair is next next nearest neighbour above the Al dopant, next nearest neighbour below the Fe dopant, and nearest neighbour in the same Cr layer as the La dopant. Frenkel defects are typically charge neutral as they are redox defects; the oxidising Cr vacancy creates holes that are filled by the reduction arising from the formation a Cr interstitial. The calculated Bader charges for each doped structures confirm this with all Cr and O species having computed charges of 4.0 e$^-$ and 7.3 e$^-$. The PEDOS plots for the Cr Frenkel defect pairs in each of the doped structures show that the holes on the O atoms arising from the Cr vacancy are filled with the appearance of the occupied O 2p defect peaks in the band gap around 0.5eV above the top of the VB.

The O Frenkel defect pair is not stable for La-Cr$_2$O$_3$ as it relaxes to a $[O_i'' + V_O^{..}]$ defect as shown in Figure 7(b). For Al-Cr$_2$O$_3$ and Fe-Cr$_2$O$_3$, the O vacancy for the oxygen Frenkel defect is nearest to the Al and Fe dopants, changing their local coordination. Al adopts a four-fold tetrahedral coordination geometry with Al-O bonds of 1.84Å (x3) and 1.88Å, and Fe has a five-fold trigonal bipyramidal geometry with Fe-O bonds of 2.06Å (x2) and 1.98Å (x3). The relative position of the O interstitial is next next nearest neighbour to the oxygen vacancy for both dopants. In Al-Cr$_2$O$_3$, the formation of an oxygen vacancy reduces a neighbouring Cr^{3+} cation to Cr^{2+} (Bader charge of 4.5 e$^-$) and the O$_i$ atom (Bader charge of 6.7 e$^-$). The corresponding spin magnetisations for the reduced Cr cation and the O$_i$ are 3.7 and 0.9 spins. The PEDOS plot with an occupied Cr 3d and O 2p defect peaks appearing in the band gap around 1.2eV above the top of the VB. For Fe-Cr$_2$O$_3$, the formation of the oxygen vacancy reduces the neighbouring Cr cation and Fe dopant to an oxidation state of +2, with computed Bader charges of 4.5 e$^-$ and 12.7 e$^-$ respectively. The spin magnetisation value of the reduced Cr cation is 3.7 spins, and the Fe dopant is 1.8 spins. The O$_i$ is not oxidised and maintains a

Bader charge of 6.3 e$^-$ with a spin magnetisation of 1.3, similar to the point O$_i$ defect. The reduction of the Cr/Fe species is seen in the PEDOS plot with the appearance of occupied Cr/Fe 3d defect peaks in the band gap around 0.8eV from the top of the VB. An occupied O 2p defect peak can also been seen in the PEDOS plot from the O$_i$ atom around 0.5eV from the top of the VB.

The Frenkel oxygen vacancy and peroxide defect is shown in Figure 7(c) along with the corresponding PEDOS plots. In all cases the oxygen vacancy and peroxide are nearest neighbour to each other and to the Fe/La dopants; the defect pair are next nearest neighbour to the Al dopant. The local bonding geometry around each of the dopants is unaffected by the defect pair, and the dopants maintain their coordination found in the non-defective metal doped Cr$_2$O$_3$. The O-O bond distance in the peroxide is 1.48Å and the Cr-O bonds to the peroxide oxygen are 2.03Å (x4). In Al-Cr$_2$O$_3$ and La-Cr$_2$O$_3$, the formation of the oxygen vacancy reduces two Cr^{3+} cations to Cr^{2+} which have computed Bader charges of 4.5 e$^-$, and both oxygen atoms in the peroxide have Bader charges of 6.7 e$^-$. The spin of each peroxide oxygen is 0 while both reduced Cr cations have opposite spins of 3.7 each. For the Fe-Cr$_2$O$_3$ structure, the oxygen vacancy reduces one Cr cation and the Fe dopant to a +2 oxidation states with computed Bader charges of 4.5 e$^-$ and 12.7 e$^-$ respectively. The Cr cation and Fe dopant have spins of 3.7 and 1.0 spins. Each of the PEDOS plots confirm the reduction process with occupied Cr 3d defect peaks appearing in the band gap around 1.3eV above the top of the VB. The peroxide O 2p contribution is mainly to the VB in Al-Cr$_2$O$_3$, however for Fe- and La-doped Cr$_2$O$_3$ an O 2p defect peak from the peroxide is seen in the band gap around 0.3eV above the top of the VB.
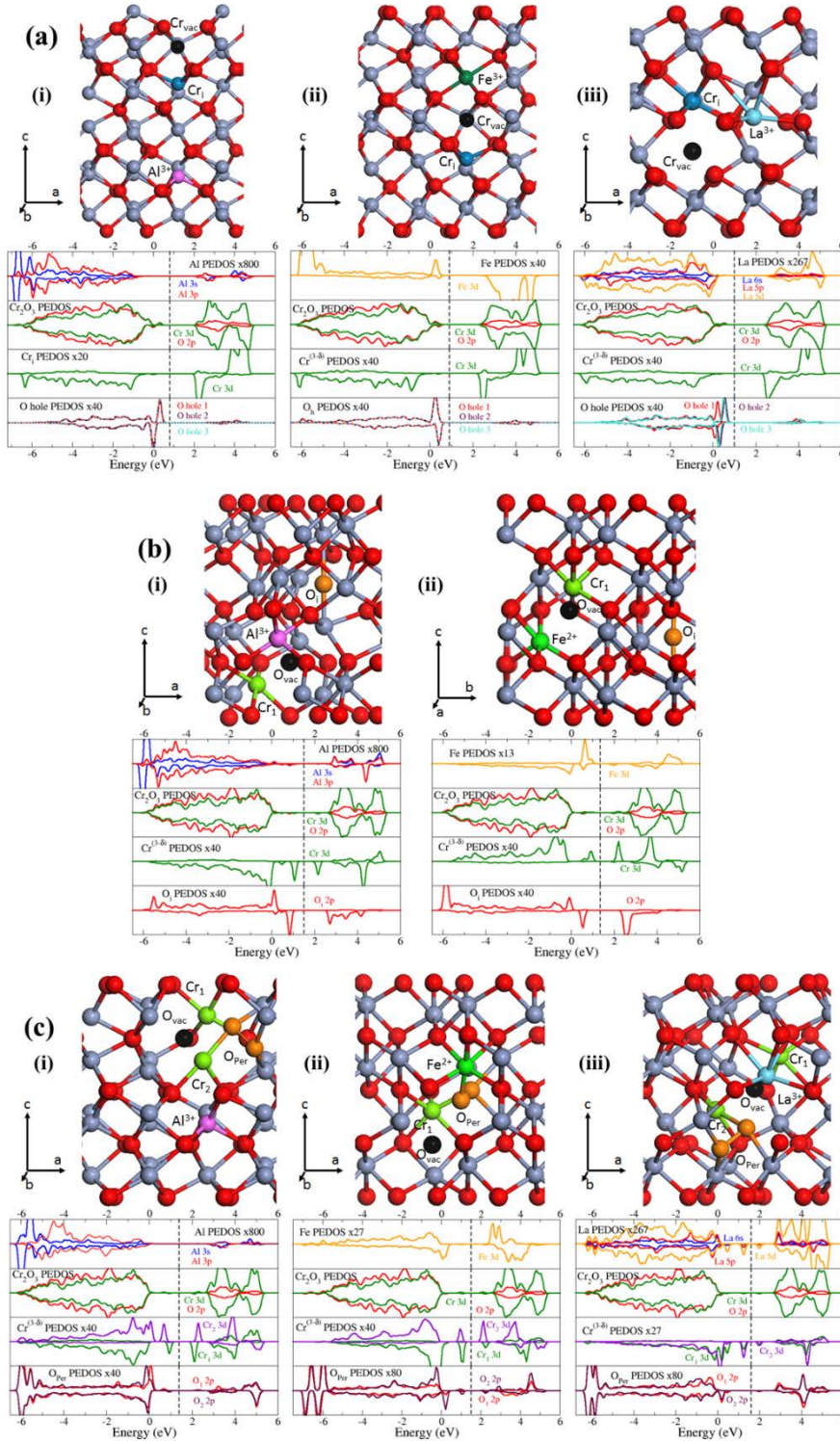
Figure 7: The calculated local geometry and PEDOS plots for (a) Cr Frenkel pair, and (b) O Frenkel pair and (c) Peroxide Frenkel pair in (i) Al-Cr_2O_3, (ii) Fe-Cr_2O_3 and (iii) La-Cr_2O_3. The grey and red spheres are the lattice Cr and O atoms, while the pink, dark green and light blue atoms are the lattice positions of the Al, Fe and La dopants. The black, light green and dark blue spheres are the lattice positions of the Cr vacancy, reduced Cr and Cr interstitial atoms, while the orange atoms are the O interstitials and peroxide atoms. The green and orange lines are the Cr and Fe/La d states, while the blue and red lines are the s and p states. The top of the valence band is aligned to 0ev in all plots and the Fermi level is indicated by the dotted line.

4.   Discussion:

The Cr/O interstitial/vacancy defects, peroxide formation and Frenkel defect pairs were investigated in undoped, Al, Fe and La doped CrO_3. For the undoped Cr_2O_3 bulk, the most favourable defect is the Cr Frenkel defect pair, consistent with previous work.[9] Previous work did not consider peroxide formation in bulk Cr_2O_3 and our calculations indicate that the peroxide defect has a similar formation energy (2.52eV) to the Cr Frenkel defect (2.34eV). This would imply that these two defects are competing in Cr_2O_3. Both are charge neutral but will have different transport capabilities. The Cr Frenkel defect is the dominant Cr defect and possibly the main cation transport carrier, while the peroxide is possibly the dominant anion defect. The low formation energy of the peroxide in Cr_2O_3 points to the potential for Cr_2O_3 to store excess oxygen in its lattice and release the oxygen when higher temperatures are achieved. The formation of excess oxygen in bulk Cr_2O_3 by peroxide defect, similarly to CeO_2 and ThO_2,[72] and the hyper-stoichiometry can be accommodated in Cr_2O_3 as the formation energy is relatively low.   The examination of the Frenkel defect, oxygen vacancy and peroxide formation shows that the peroxide is stable even when vacancies are present in the bulk which is not seen for CeO_2 and ThO_2.[72] This may indicate that Cr_2O_3 has the potential to readily store excess oxygen at higher operating temperatures and not fill oxygen vacancies that may kill the ionic conductivity.   This is an important property for OSC materials and also as an oxygenation catalyst which could potentially supply excess oxygen atoms to the surface for oxygenation reactions such as methanol synthesis and water gas shift reactions,[89] and to improve protective coatings.[19, 30]

The doping of Cr_2O_3 with Al changes the local geometric and electronic structure of the bulk and the defects, but does not significantly change the formation energies for all the defects studied. The exception is the O Frenkel defect, which has an increased formation energy. The dominant defect for Al-Cr_2O_3 is the Cr Frenkel pair with the peroxide defect is also a competing

process. Fe doping does not greatly enhance the formation energy of oxygen vacancies and the defect with the lowest formation energy is also the Cr Frenkel defect pair. However the Fe dopant notably increases the formation energies of the other defects (oxygen interstitial, peroxide, Cr vacancies), so that they are no longer competing with the O vacancy formation. This would indicate that Fe doping can improve the reducibility of Cr_2O_3 and thus the OSC properties. Since the Fe dopant greatly increases the formation energies for the O interstitial and peroxide Frenkel defect pairings, this indicates that oxygen vacancy formation could occur without formation of interstitials or peroxides which would otherwise kill the O vacancies.

The large La dopant cation in the Cr_2O_3 lattice greatly promotes Cr vacancy and Cr Frenkel defect formation, but does not significantly improve the oxygen vacancy or peroxide formation in the Cr_2O_3 bulk. The promoting effect of the La doping on cation vacancies in the bulk may be useful for p-type conduction as the La-Cr_2O_3 more easily generates holes. However, the low formation energy of the Cr Frenkel defect pair does suggest that the holes could be killed by the formation of the Cr interstitial close to the Cr vacancy. The utility of La doping in Cr_2O_3 is worthy of attention, in particular for charged defect formation which is however beyond the scope of this work.

In contrast to aliovalent dopants,[15] the presence of the isovalent dopants in bulk Cr_2O_3 does not greatly improve the reducibility of the material. We suggest that the isovalent dopants do not introduce sufficient structural distortions and charge compensating vacancies, when compared to lower valence dopants. These distortions generally appear to be important in ensuring higher reducibility in doped metal oxides, as also seen for CeO_2 and TiO_2.[35, 36, 39, 40, 45, 46] The dopants do however introduce interesting changes to the bulk properties of the material. Fe doping can suppress defects that compete with oxygen vacancies, while La doping can enhance cation defect formation. These have beneficial implications in catalysis as competing processes that could potentially kill desired defects such as oxygen vacancies in

oxygenation catalysis or the cathode of an SOFC can be suppressed, and enhance cation vacancies in the bulk may be useful in semiconducting properties required for oxygen transport.

5.   Conclusion:

Density functional theory calculations with a Hubbard +U correction applied to the Cr 3d and O 2p states were used to investigated the formation of Cr/O vacancies/interstitials and Frenkel defect pairs in undoped, Al, Fe and La doped Cr_2O_3. For undoped Cr_2O_3, the dominant defects are the peroxide and Cr Frenkel defect pair which have similar formation energies and can be competing processes in the bulk lattice. Al doping does not significantly alter any of the defect formation energies. Fe doping in Cr_2O_3 does not promote any of the defects under consideration, however it does greatly increase the formation energy of oxygen interstitial and peroxide defects, suppressing their formation which may assist in forming the dominant defects such as oxygen vacancies. Also Fe undergoes reduction in addition to Cr which may promote reducibility in the material without killing conductivity. For La-Cr_2O_3, the formation of Cr vacancies and Cr Frenkel defect pair are promoted by the presence of the La dopant.

6.   Acknowledgements:

7.   References:

1.   Kushima, A. and B. Yildiz, *Oxygen ion diffusivity in strained yttria stabilized zirconia: where is the fastest strain?* J. Mater. Chem., 2010. **20**: p. 11.
2.   Seymour, I.D., et al., *Defect processes in orthorhombic LnBaCo2O5.5 double perovskites.* Physical Chemistry Chemical Physics, 2011. **13**(33): p. 15305-15310.
3.   Seymour, I.D., et al., *Anisotropic oxygen diffusion in PrBaCo2O5.5 double perovskites.* Solid State Ionics, 2012. **216**: p. 41-43.
4.   Popovici, N., et al., *KrF Pulsed Laser Deposition of Chromium Oxide Thin Films from Cr_8O_{21} Targets.* Applied Physics A: Materials Science and Processing, 2004. **79**(4-6): p. 1409-1411.
5.   Corliss, L.M., et al., *Magnetic Structure of Cr_2O_3.* Journal of Applied Physics, 1965. **36**(3): p. 1099-1100.
6.   Brown, P.J., et al., *Determination of the Magnetization Distribution in Cr_2O_3 using Spherical Neutron Polarimetry.* Journal of Physics: Condensed Matter, 2002. **14**(8): p. 1957.
7.   Zimmermann, R., P. Steiner, and S. Hüfner, *Electron Spectroscopies and Partial Excitation Spectra in Cr_2O_3*, in *Proc. 11th Intern. Conf. Vac. UV Rad. Phys.* , T. Miyahara, et al., Editors. 1996, Elsevier: Amsterdam. p. 49-52.
8.   Uozumi, T., K. Okada, and A. Kotani, *Theory of Photoemission Spectra for M_2O_3 (M= Ti, V, Cr, Mn, Fe) Compounds.* Journal of Electron Spectroscopy and Related Phenomena, 1996. **78**: p. 103-106.
9.   Lebreau, F., et al., *Structural, Magnetic, Electronic, Defect, and Diffusion Properties of Cr_2O_3: A DFT+U Study.* The Journal of Physical Chemistry C, 2014. **118**(31): p. 18133-18145.
10.   Maldonado, F., R. Rivera, and A. Stashans, *Structure, Electronic and Magnetic Properties of Ca-doped Chromium Oxide Studied by the DFT Method.* Physica B: Condensed Matter, 2012. **407**(8): p. 1262-1267.
11.   Maldonado, F., C. Novillo, and A. Stashans, *Ab Initio Calculation of Chromium Oxide Containing Ti Dopant.* Chemical Physics, 2012. **393**(1): p. 148-152.
12.   Rollmann, G., et al., *First-principles Calculation of the Structure and Magnetic Phases of Hematite.* Physical Review B, 2004. **69**(16): p. 165107.
13.   Rohrbach, A., J. Hafner, and G. Kresse, *Ab initio Study of the (0001) Surfaces of Hematite and Chromia: Influence of Strong Electronic Correlations.* Physical Review B, 2004. **70**(12): p. 125426.
14.   Kehoe, A.B., et al., *Assessing the Potential of Mg-doped Cr_2O_3 as a Novel P-type Transparent Conducting Oxide.* Journal of Physics: Condensed Matter, 2016. **28**(12): p. 125501.
15.   Carey, J.J., M. Legesse, and M. Nolan, *Low Valence Cation Doping of Bulk Cr2O3: Charge Compensation and Oxygen Vacancy Formation.* The Journal of Physical Chemistry C, 2016. **120**(34): p. 19160-19174.
16.   Guo, Y., S.J. Clark, and J. Robertson, *Electronic and Magnetic Properties of Ti_2O_3 , Cr_2O_3 , and Fe_2O_3 Calculated by the Screened Exchange Hybrid Density Functional.* Journal of Physics: Condensed Matter, 2012. **24**(32): p. 325504.
17.   Catlow, C.R.A., et al., *Atomistic Simulation of Defect Structures and Ion Transport in α-Fe_2O_3 and α-Cr_2O_3.* Journal of the American Ceramic Society, 1988. **71**(1): p. 42-49.
18.   Brady, M.P., et al., *Comparison of Oxidation Behavior and Electrical Properties of Doped NiO- and Cr_2O_3 -Forming Alloys for Solid-Oxide, Fuel-Cell Metallic Interconnects.* Oxidation of Metals, 2006. **65**(3-4): p. 237-261.
19.   Matsuzaki, Y. and I. Yasuda, *Dependence of SOFC Cathode Degradation by Chromium-containing Alloy on Compositions of Electrodes and Electrolytes.* Journal of The Electrochemical Society, 2001. **148**(2): p. A126-A131.

20. Nakayama, O., et al., *Production of Synthesis Gas from Methane Using Lattice Oxygen of NiO−Cr$_2$O$_3$−MgO Complex Oxide.* Industrial and Engineering Chemistry Research, 2010. **49**(2): p. 526-534.

21. El-Molla, S.A., *Surface and Catalytic Properties of Cr$_2$O$_3$/MgO System Doped with Manganese and Cobalt Oxides.* Applied Catalysis A: General, 2005. **280**(2): p. 189-197.

22. Calverley, E.M. and K.J. Smith, *Kinetic Model for Alcohol Synthesis over a Promoted Copper/Zinc Oxide/Chromium Oxide (Cr$_2$O$_3$) Catalyst.* Industrial and Engineering Chemistry Research, 1992. **31**(3): p. 792-803.

23. Cline, J.A., A.A. Rigos, and T.A. Arias, *Ab Initio Study of Magnetic Structure and Chemical Reactivity of Cr$_2$O$_3$ and Its (0001) Surface.* The Journal of Physical Chemistry B, 2000. **104**(26): p. 6195-6201.

24. Beretta, A., et al., *Production of Methanol and Isobutyl Alcohol Mixtures over Double-bed Cesium-promoted Cu/ZnO/Cr$_2$O$_3$ and ZnO/Cr$_2$O$_3$ catalysts.* Industrial and engineering chemistry research, 1996. **35**(5): p. 1534-1542.

25. Mehta, S., et al., *Catalytic Synthesis of Methanol from COH2: II. Electron microscopy (TEM, STEM, microdiffraction, and energy dispersive analysis) of the CuZnO and Cu/ZnO/Cr$_2$O$_3$ Catalysts.* Journal of Catalysis, 1979. **57**(3): p. 339-360.

26. Borck, Ø. and E. Schröder, *Adsorption of Methanol and Methoxy on the α-Cr$_2$O$_3$ (0001) surface.* Journal of Physics: Condensed Matter, 2006. **18**(48): p. 10751.

27. Hu, J., et al., *Improve the Electrochemical Performances of Cr$_2$O$_3$ Anode for Lithium Ion Batteries.* Solid State Ionics, 2006. **177**(26–32): p. 2791-2799.

28. Huang, R.F., A.K. Agarwal, and H.U. Anderson, *Oxygen Activity Dependence of the Electrical Conductivity of Li-Doped Cr$_2$O$_3$.* Journal of the American Ceramic Society, 1984. **67**(2): p. 146-150.

29. Kohli, N., O. Singh, and R. Singh, *Sensing Behaviour of Tin Doped Chromium Oxide Gas Sensor Toward Ethanol.* Applied Physics A, 2012. **109**(3): p. 585-590.

30. Chen, X., et al., *Protective Coating on Stainless Steel Interconnect for SOFCs: Oxidation Kinetics and Electrical Properties.* Solid State Ionics, 2005. **176**(5): p. 425-433.

31. Liu, Y. and D. Chen, *Protective Coatings for Cr$_2$O$_3$ -Forming Interconnects of Solid Oxide Fuel Cells.* international journal of hydrogen energy, 2009. **34**(22): p. 9220-9226.

32. Xiao, M., et al., *Improvement of Electromigration Reliability and Diffusion of Cu Films using Coherent Cu (111)/Cr$_2$O$_3$ (0001) Interfaces.* Chemical Physics Letters, 2012. **542**: p. 85-88.

33. Batzill, M., E.H. Morales, and U. Diebold, *Influence of Nitrogen Doping on the Defect Formation and Surface Properties of TiO$_2$ Rutile and Anatase.* Physical review letters, 2006. **96**(2): p. 026103.

34. Gordon, T.R., et al., *Nonaqueous Synthesis of TiO$_2$ Nanocrystals using TiF$_4$ to Engineer Morphology, Oxygen Vacancy Concentration, and Photocatalytic Activity.* Journal of the American Chemical Society, 2012. **134**(15): p. 6751-6761.

35. Iwaszuk, A. and M. Nolan, *Electronic Structure and Reactivity of Ce-and Zr-Doped TiO$_2$: Assessing the Reliability of Density Functional Theory Approaches.* The Journal of Physical Chemistry C, 2011. **115**(26): p. 12995-13007.

36. Iwaszuk, A. and M. Nolan, *Charge Compensation in Trivalent Cation Doped Bulk Rutile TiO$_2$.* Journal of Physics: Condensed Matter, 2011. **23**(33): p. 334207.

37. Nakamura, I., et al., *Role of Oxygen Vacancy in the Plasma-treated TiO$_2$ Photocatalyst with Visible Light Activity for NO Removal.* Journal of Molecular Catalysis A: Chemical, 2000. **161**(1): p. 205-212.

38. Schaub, R., et al., *Oxygen-mediated Diffusion of Oxygen Vacancies on the TiO$_2$ (110) Surface.* Science, 2003. **299**(5605): p. 377-379.

39. Carey, J.J. and M. Nolan, *Dissociative Adsorption of Methane on the Cu and Zn Doped (111) Surface of CeO$_2$.* Applied Catalysis B: Environmental, 2016. **197**: p. 324-336.

40. Carey, J.J. and M. Nolan, *Cation Doping Size Effect for Methane Activation on Alkaline Earth Metal Doping of the CeO$_2$ (111) Surface.* Catalysis Science & Technology, 2016. **6**(10): p. 3544-3558.

41. Fornasiero, P., et al., *Rh-loaded CeO$_2$ -ZrO$_2$ Solid-solutions as Highly Efficient Oxygen Exchangers: Dependence of the Reduction Behavior and the Oxygen Storage Capacity on the Structural-properties.* Journal of Catalysis, 1995. **151**(1): p. 168-177.

42. Kehoe, A.B., D.O. Scanlon, and G.W. Watson, *Role of Lattice Distortions in the Oxygen Storage Capacity of Divalently Doped CeO$_2$.* Chemistry of Materials, 2011. **23**(20): p. 4464-4468.

43. Keating, P.R., D.O. Scanlon, and G.W. Watson, *The Nature of Oxygen States on the Surfaces of CeO$_2$ and La-doped CeO$_2$.* Chemical Physics Letters, 2014. **608**: p. 239-243.

44. Keating, P.R., D.O. Scanlon, and G.W. Watson, *Computational Testing of Trivalent Dopants in CeO$_2$ for Improved High-κ Dielectric Behaviour.* Journal of Materials Chemistry C, 2013. **1**(6): p. 1093-1098.

45. Nolan, M., *Charge Compensation and Ce^{3+} Formation in Trivalent Doping of the CeO$_2$ (110) Surface: The Key Role of Dopant Ionic Radius.* The Journal of Physical Chemistry C, 2011. **115**(14): p. 6671-6681.

46. Nolan, M., *Enhanced Oxygen Vacancy Formation in Ceria (111) and (110) surfaces Doped with Divalent Cations.* Journal of Materials Chemistry, 2011. **21**(25): p. 9160-9168.

47. Atkinson, K.J.W., et al., *Accommodation of impurities in α-Al2O3, α-Cr2O3 and α-Fe2O3.* Journal of the European Ceramic Society, 2003. **23**(16): p. 3059-3070.

48. Qin, P., et al., *Organic Solar Cells with P-type Amorphous Chromium Oxide Thin Film as Hole-transporting Layer.* Thin Solid Films, 2011. **519**(13): p. 4334-4341.

49. Qin, P., et al., *Nitrogen Doped Amorphous Chromium Oxide: Stability Improvement and Application for the Hole-transporting Layer of Organic Solar Cells.* Solar Energy Materials and Solar Cells, 2011. **95**(3): p. 1005-1010.

50. Cao, H., et al., *Sol-gel Synthesis and Photoluminescence of P-type Semiconductor Cr$_2$O$_3$ Nanowires.* Applied Physics Letters, 2006. **88**(24): p. 241112.

51. Choi, S.-Y., M.-H. Kim, and Y.-U. Kwon, *Effects of Cr$_2$O$_3$ Modification on the Performance of SnO$_2$ Electrodes in DSSCs.* Physical Chemistry Chemical Physics, 2012. **14**(10): p. 3576-3582.

52. Farrell, L., et al., *Conducting Mechanism in the Epitaxial P-type Transparent Conducting Oxide Cr$_2$O$_3$: Mg.* Physical Review B, 2015. **91**(12): p. 125202.

53. Arca, E., K. Fleischer, and I.V. Shvets, *Magnesium, Nitrogen Co-doped Cr$_2$O$_3$: A P-type Transparent Conducting Oxide.* Applied Physics Letters, 2011. **99**(11): p. 111910.

54. Arca, E., et al., *Effect of Chemical Precursors On the Optical and Electrical Properties of P-type Transparent Conducting Cr$_2$O$_3$: (Mg,N).* The Journal of Physical Chemistry C, 2013. **117**(42): p. 21901-21907.

55. Goel, S., et al., *Structural, Optical and Magnetic Properties of Fe Doped Cr$_2$O$_3$ Nanoparticles.* Advanced Science Letters, 2014. **20**(7-8): p. 1562-1566.

56. Chroneos, A., C.A. Londos, and H. Bracht, *A-centers and isovalent impurities in germanium: Density functional theory calculations.* Materials Science and Engineering: B, 2011. **176**(5): p. 453-457.

57. Li, J. and S.-H. Wei, *Alignment of isovalent impurity levels: Oxygen impurity in II-VI semiconductors.* Physical Review B, 2006. **73**(4): p. 041201.

58. Singh, K., et al., *A study of iso- and alio-valent cation doped Ag2SO4 solid electrolyte.* Applied Physics A, 1998. **66**(2): p. 205-215.

59. Vinodkumar, T., B.G. Rao, and B.M. Reddy, *Influence of isovalent and aliovalent dopants on the reactivity of cerium oxide for catalytic applications.* Catalysis Today, 2015. **253**: p. 57-64.

60. Trovarelli, A., *Structural and Oxygen Storage/Release Properties of CeO2-Based Solid Solutions.* Comments on Inorganic Chemistry, 1999. **20**(4-6): p. 263-284.

61.   Tang, Y., et al., *First-principles investigation on redox properties of M-doped ${\text{CeO}}_{2}$ $(M=\text{Mn},\text{Pr},\text{Sn},\text{Zr})$.* Physical Review B, 2010. **82**(12): p. 125104.

62.   Tealdi, C., et al., *Defect and dopant properties of MgTa2O6.* Journal of Solid State Chemistry, 2004. **177**(11): p. 4359-4367.

63.   Fu, Z., et al., *Surface treatment with Al3+on a Ti-doped [small alpha]-Fe2O3 nanorod array photoanode for efficient photoelectrochemical water splitting.* Journal of Materials Chemistry A, 2014. **2**(33): p. 13705-13712.

64.   Xia, C., et al., *Tuning the band gap of hematite α-Fe2O3 by sulfur doping.* Physics Letters A, 2013. **377**(31–33): p. 1943-1947.

65.   Aschauer, U., J. Chen, and A. Selloni, *Peroxide and superoxide states of adsorbed O2 on anatase TiO2 (101) with subsurface defects.* Physical Chemistry Chemical Physics, 2010. **12**(40): p. 12956-12960.

66.   Pushkarev, V.V., V.I. Kovalchuk, and J.L. d'Itri, *Probing Defect Sites on the CeO2 Surface with Dioxygen.* The Journal of Physical Chemistry B, 2004. **108**(17): p. 5341-5348.

67.   Zhao, Y., et al., *Superoxide and Peroxide Species on CeO2(111), and Their Oxidation Roles.* The Journal of Physical Chemistry C, 2012. **116**(30): p. 15986-15991.

68.   Machida, M., et al., *On the Reasons for High Activity of CeO2 Catalyst for Soot Oxidation.* Chemistry of Materials, 2008. **20**(13): p. 4489-4494.

69.   Trovarelli, A., *Catalytic properties of ceria and CeO2-containing materials.* Catalysis Reviews, 1996. **38**(4): p. 439-520.

70.   Middleburgh, S.C., K.P.D. Lagerlof, and R.W. Grimes, *Accommodation of Excess Oxygen in Group II Monoxides.* Journal of the American Ceramic Society, 2013. **96**(1): p. 308-311.

71.   Middleburgh, S.C., et al., *Peroxide defect formation in zirconate perovskites.* Journal of Materials Chemistry A, 2014. **2**(38): p. 15883-15888.

72.   Middleburgh, S.C., G.R. Lumpkin, and R.W. Grimes, *Accommodation of excess oxygen in fluorite dioxides.* Solid State Ionics, 2013. **253**: p. 119-122.

73.   Perdew, J.P. and W. Yue, *Accurate and Simple Density Functional for the Electronic Exchange Energy: Generalized Gradient Approximation.* Physical review B, 1986. **33**(12): p. 8800.

74.   Perdew, J.P., K. Burke, and M. Ernzerhof, *Generalized Gradient Approximation Made Simple.* Physical review letters, 1996. **77**(18): p. 3865.

75.   Kresse, G. and J. Furthmüller, *Efficiency of Ab-initio Total Energy Calculations for Metals and Semiconductors using a Plane-wave Basis Set.* Computational Materials Science, 1996. **6**(1): p. 15-50.

76.   Kresse, G. and J. Furthmüller, *Software VASP, Vienna (1999).* Phys. Rev. B, 1996. **54**(11): p. 169.

77.   Kresse, G. and J. Furthmüller, *Efficient Iterative Schemes for Ab-initio Total-energy Calculations using a Plane-wave Basis Set.* Physical Review B, 1996. **54**(16): p. 11169.

78.   Kresse, G. and D. Joubert, *From Ultrasoft Pseudopotentials to the Projector Augmented-wave Method.* Physical Review B, 1999. **59**(3): p. 1758.

79.   Kresse, G. and J. Hafner, *Norm-conserving and ultrasoft pseudopotentials for first-row and transition elements.* Journal of Physics: Condensed Matter, 1994. **6**(40): p. 8245.

80.   Dudarev, S.L., et al., *Surface States on NiO (100) and the Origin of the Contrast Reversal in Atomically Resolved Scanning Tunneling Microscope Images.* Physical Review B, 1997. **56**(8): p. 4900-4908.

81.   Dudarev, S., et al., *Electron-Energy-Loss Spectra and the Structural Stability of Nickel Oxide: An LSDA+U study.* Physical Review B, 1998. **57**(3): p. 1505.

82.   Monkhorst, H.J. and J.D. Pack, *Special Points for Brillouin-zone Integrations.* Physical Review B, 1976. **13**(12): p. 5188.

83.   Murnaghan, F., *The Compressibility of Media Under Extreme Pressures.* Proceedings of the national academy of sciences of the United States of America, 1944. **30**(9): p. 244.

84.   Di Cerbo, R.K. and A.U. Seybolt, *Lattice Parameters of the α-Fe$_2$O$_3$-Cr$_2$O$_3$ Solid Solution.* Journal of the American Ceramic Society, 1959. **42**(9): p. 430-431.

85.   Tang, W., E. Sanville, and G. Henkelman, *A grid-based Bader analysis algorithm without lattice bias.* Journal of Physics: Condensed Matter, 2009. **21**(8): p. 084204.

86.   Sanville, E., et al., *Improved grid-based algorithm for Bader charge allocation.* Journal of computational chemistry, 2007. **28**(5): p. 899-908.

87.   Henkelman, G., A. Arnaldsson, and H. Jónsson, *A fast and robust algorithm for Bader decomposition of charge density.* Computational Materials Science, 2006. **36**(3): p. 354-360.

88.   Arnaldsen, A., W. Tang, and G. Henkelman, *Bader charge analysis.* 2012.

89.   Mierczynski, P., et al., *Cu/Cr2O3·3Al2O3 and Au–Cu/Cr2O3·3Al2O3 catalysts for methanol synthesis and water gas shift reactions.* Reaction Kinetics, Mechanisms and Catalysis, 2011. **104**(1): p. 139-148.